Particles I

Access the latest eBook →

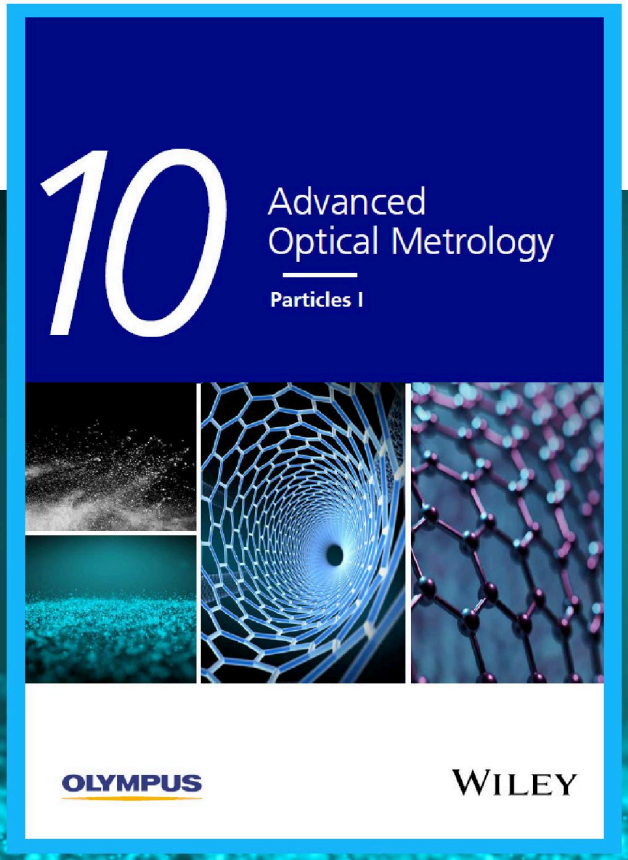

Particles: Unique Properties, Uncountable Applications

Read the latest eBook and better your knowledge with highlights from the recent studies on the design and characterization of micro- and nanoparticles for different application areas.

Access Now

This eBook is sponsored by

OLYMPUS®

WILEY

ADVANCED FUNCTIONAL MATERIALS
www.afm-journal.de

Check for updates

Accelerated Discovery and Design of Ultralow Lattice Thermal Conductivity Materials Using Chemical Bonding Principles

Jiangang He, Yi Xia, Wenwen Lin, Koushik Pal, Yizhou Zhu, Mercouri G. Kanatzidis, and Chris Wolverton**

Semiconductors with very low lattice thermal conductivities are highly desired for applications relevant to thermal energy conversion and management, such as thermoelectrics and thermal barrier coatings. Although the crystal structure and chemical bonding are known to play vital roles in shaping heat transfer behavior, material design approaches of lowering lattice thermal conductivity using chemical bonding principles are uncommon. In this work, an effective strategy of weakening interatomic interactions and therefore suppressing lattice thermal conductivity based on chemical bonding principles is presented and a high-efficiency approach of discovering low κ_L materials by screening the local coordination environments of crystalline compounds is developed. The resulting first-principles calculations uncover 30 hitherto unexplored compounds with (ultra)low lattice thermal conductivities from 13 prototype crystal structures contained in the Inorganic Crystal Structure Database. Furthermore, an approach of rationally designing high-performance thermoelectrics is demonstrated by additionally incorporating cations with stereochemically active lone-pair electrons. These results not only provide atomic-level insights into the physical origin of the low lattice thermal conductivity in a large family of copper/silver-based compounds but also offer an efficient approach to discover and design materials with targeted thermal transport properties.

1. Introduction

Crystalline solids with very low lattice thermal conductivities (κ_L) are both fundamentally interesting and technologically important in generating, converting, and managing thermal energy.[1–3] In the simple kinetic theory,[4] $\kappa_L = \frac{1}{3} C v_g^2 \tau$, where C, v_g, and τ are heat capacity, phonon group velocity (v_g), and phonon relaxation time (τ), respectively. Therefore, materials with low v_g, short τ, or small C usually have low κ_L. Decades of studies on thermoelectric materials have explored many strategies of designing and discovering new materials with low κ_L, as well as minimizing κ_L of well-studied materials.[5–7] The widely used approaches that can effectively shorten τ are based on introducing defects,[6] nano-structure precipitates,[8–11] lone-pair electrons ions,[12,13] rattling phonon modes,[14–18] and ferroelectric instability-induced phonon softening.[19,20] Since v_g is proportional to $\sqrt{k/M}$, where k and M are respectively the bond stiffness (or bond strength) and the atomic mass,[4] low v_g are also expected in materials with weak chemical bonds and large atomic masses. Taking advantage of the large atomic mass is straightforward and has been utilized to screen new thermoelectric materials with low κ_L recently.[21] However, bond strength is more complicated and correlated to the electronegativities of constituent atoms and local coordination of a crystal structure. Generally, the bond in the environment with a higher coordination number (CN) is weaker than that in a lower CN one due to the longer bond length between cation and anion in the high CN case, reflecting Pauling's second rule.[22] For example, the bond length in the rock-salt structure (octahedral coordination, CN = 6) is usually longer than that in the zinc blende structure (tetrahedral coordination, CN = 4). As a consequence, the rock-salt compounds (e.g., NaCl: 7.1 $Wm^{-1} K^{-1}$, RbCl: 2.8 $Wm^{-1} K^{-1}$ at 300 K[23]) usually have much lower κ_L than the zinc blende ones (e.g., GaAs: 45 $Wm^{-1} K^{-1}$, ZnSe: 19 $Wm^{-1} K^{-1}$ at 300 K).[24–26] On the other hand, since the wurtzite-type structure has the same local coordination with the zinc blende (the only difference is the

J. He, Y. Xia, K. Pal, Y. Zhu, C. Wolverton
Department of Materials Science and Engineering
Northwestern University
Evanston, IL 60208, USA
E-mail: c-wolverton@northwestern.edu

J. He
School of Mathematics and Physics
University of Science and Technology Beijing
Beijing 100083, China
E-mail: jghe2021@ustb.edu.cn

W. Lin, M. G. Kanatzidis
Department of Chemistry
Northwestern University
Evanston, IL 60208, USA

W. Lin
Engineering Laboratory of Advanced Energy Materials
Ningbo Institute of Industrial Technology
Chinese Academy of Sciences
Ningbo, Zhejiang 315201, China

The ORCID identification number(s) for the author(s) of this article can be found under https://doi.org/10.1002/adfm.202108532.

DOI: 10.1002/adfm.202108532

 © 2021 Wiley-VCH GmbH

stacking ordering), wurtzite compounds have very similar κ_L as zinc blende.[26,27]

Surprisingly, a few copper and silver-based compounds with the zinc blende structure and small average atomic masses ($\overline{M}$ = 49–95) show unexpectedly low κ_L. For instance, the κ_L of CuCl, CuBr, and CuI are 0.84, 1.25, 1.68 Wm^{-1} K^{-1} at 300 K, respectively,[28,29] which are even lower than the heavier ($\overline{M}$ = 167), rock-salt, and strongly anharmonic compound PbTe.[19,30] Compared to the conventional zinc blende compounds, these compounds display unique lattice dynamics properties, featuring low-frequency dispersions and soft optical modes, which have been attributed to the large ionic radius mismatch between Cu^+ and Cl^- ions.[31] Meanwhile, experiments have shown a large thermal displacement parameter of Cu in CuCl,[32] indicating a weak Cu-Cl bond and corroborating the existence of low-frequency phonons. Another set of interesting compounds include β-$BaCu_2S_2$, which crystallizes in the $ThCr_2Si_2$-type structure and possesses an ultralow κ_L of 0.68 Wm^{-1} K^{-1} at 300 K[33] and BiCuSeO, which adopts the ZrCuSiAs-type structure and has a κ_L of 1.0 Wm^{-1} K^{-1} at 300 K.[34] The common feature of these two structures is the presence of the edge-sharing CuX_4 (X = S and Se) tetrahedra. It is interesting to note that all the listed compounds contain Cu, which, akin to Ag, often forms superionic conductors at high temperatures due to the weak chemical bond between Cu^+/Ag^+ and anions.[32,35] Considering the facts that i) Cu is an abundant earth element and the synthesis of Cu-based compounds is relatively easy, and ii) Cu-based thermoelectric materials have a long research history back to 1827, and many of them have good thermoelectric performance,[34,36–43] it is intriguing to ask what makes the thermal transport behaviors of these compounds so anomalous?

These observations motivate us to investigate the origin of low κ_L and its relation to the distinctive chemical bonds in Cu/Ag-based compounds and to ultimately search for new materials with very low κ_L by exploiting the underlying mechanisms. We find that the intrinsically low κ_L of these compounds is mainly attributable to the weak bonds between Cu/Ag and anions, originating from the antibonding interactions between Cu/Ag-*d* orbitals and anion-*p* orbitals through an unusual *p*-*d* coupling.[44,45] Moreover, we demonstrate that the antibonding interaction can be further weakened by introducing edge-sharing and face-sharing polyhedra centered at Cu^+/Ag^+, in the spirit of Pauling's third rule.[22] Based on these findings, we then perform a comprehensive screening for compounds exhibiting these local coordination environments within the Inorganic Crystal Structure Database (ICSD). We discovered 30 hitherto unexplored compounds that potentially exhibit very low κ_L, as evidenced by our first-principles anharmonic lattice dynamics simulations. To further improve these compounds for thermoelectric applications, we also propose a general strategy of improving electrical transport properties by incorporating cations with stereochemically active lone-pair electrons. The materials design philosophy based on the crystal and structural chemistry unveiled by this study is extendable to a broad classe of materials systems, and hence should aid the rational design of thermal management materials and thermoelectric materials.

2. Results

2.1. Design Strategy I: Antibonding from *p*-*d* Hybridization

To understand the unusually low κ_L identified in the copper-based compounds from chemical bonding, we compare and analyze the electronic structures of three representative zinc blende compounds, namely CuBr, ZnSe, and GaAs, which show drastically different κ_L with values of 1.25, 19, and 45 Wm^{-1} K^{-1} at 300 K, respectively. One particular reason of choosing these three compounds is that they have nearly the same $\overline{M}$ (≈72 amu.), thus ensuring that the vastly different κ_L is not simply due to atomic mass. In **Figure 1**, we show their orbital-projected band structures, the crystal orbital Hamilton population (COHP), and the corresponding molecular orbital diagrams, respectively. These three compounds have similar band structures, where the three-fold degenerate valence band maximum (VBM) is located at the Γ point. However, the characters of these bands are very different: the VBM of CuBr has more *d*-orbital contribution than ZnSe and GaAs has no *d*-orbitals at all. This can be explained by the *p*-*d* hybridization discovered by Jaffe et al.[44] and Wei et al.,[45] which states that the filled 3*d* orbitals of Zn^{2+} and Cu^+ (d^{10} configuration) can participate in bonding with the 4*p* orbitals of Se and Br in the zinc blende ZnSe and CuBr, due to the inversion-symmetry breaking of $ZnSe_4$ tetrahedron (or in general MX_4 tetrahedron, where M and X are cation and anion, respectively). In contrast, the *p*-*d* coupling is prohibited in the case of MX_6 octahedron as in the rock-salt structure because the odd (*d*) and even (*p*) angular momentum cannot mix in the presence of inversion symmetry.[44,45] The hybridization between the filled *M*-*d* and *X*-*p* orbitals forms *p*-*d* bonding and *p*-*d** antibonding states just below the Fermi level. Importantly, the occupation of the *p*-*d** antibonding states would naturally destabilize the *M*-*X* bond strength, due to the decrease of the bond order. They further show that the overlap (strength of hybridization) between *M*-*d* and *X*-*p* orbitals depends on the energy difference of the constituent ions' orbitals, provided that the *p*-*d* coupling is allowed by symmetry.

Based on these findings, we examine the trend of chemical bonding from CuBr to ZnSe and GaAs, wherein the energy difference between *M*-3*d* and *X*-4*p* orbitals increases. As we can see from the orbital mixing in Figure 1, the hybridization between *M*-*d* and *X*-*p* orbitals in these compounds decreases rapidly from CuBr to GaAs. Such a trend can be understood as follows: i) In these three compounds, the *M*-3*d* orbitals split into t_{2g} and e_g levels under the tetrahedral crystal field; ii) for the cases of CuBr and ZnSe, the t_{2g} orbitals hybridize with *X*-4*p* and form bonding and antibonding states below the Fermi level, while the e_g orbitals hardly interact with *X*-4*p* and form non-bonding states, (see Figure 1a,b); iii) since Cu-3*d* orbitals are higher in energy than Br-4*p*, the *p*-*d* antibonding states in CuBr are dominated by the Cu-3*d* orbitals and the bonding states are mainly from Br-4*p* (see Figure 1a). In contrast, Se-4*p* orbitals have a larger contribution to the *p*-*d* antibonding states than Zn-3*d* in ZnSe (see Figure 1b), due to the lower energy level of Zn-3*d* than Se-4*p*; and iv) in the case of GaAs, the Ga-3*d* is too deep to interact with As-4*p* and therefore, there is almost no

© 2021 Wiley-VCH GmbH

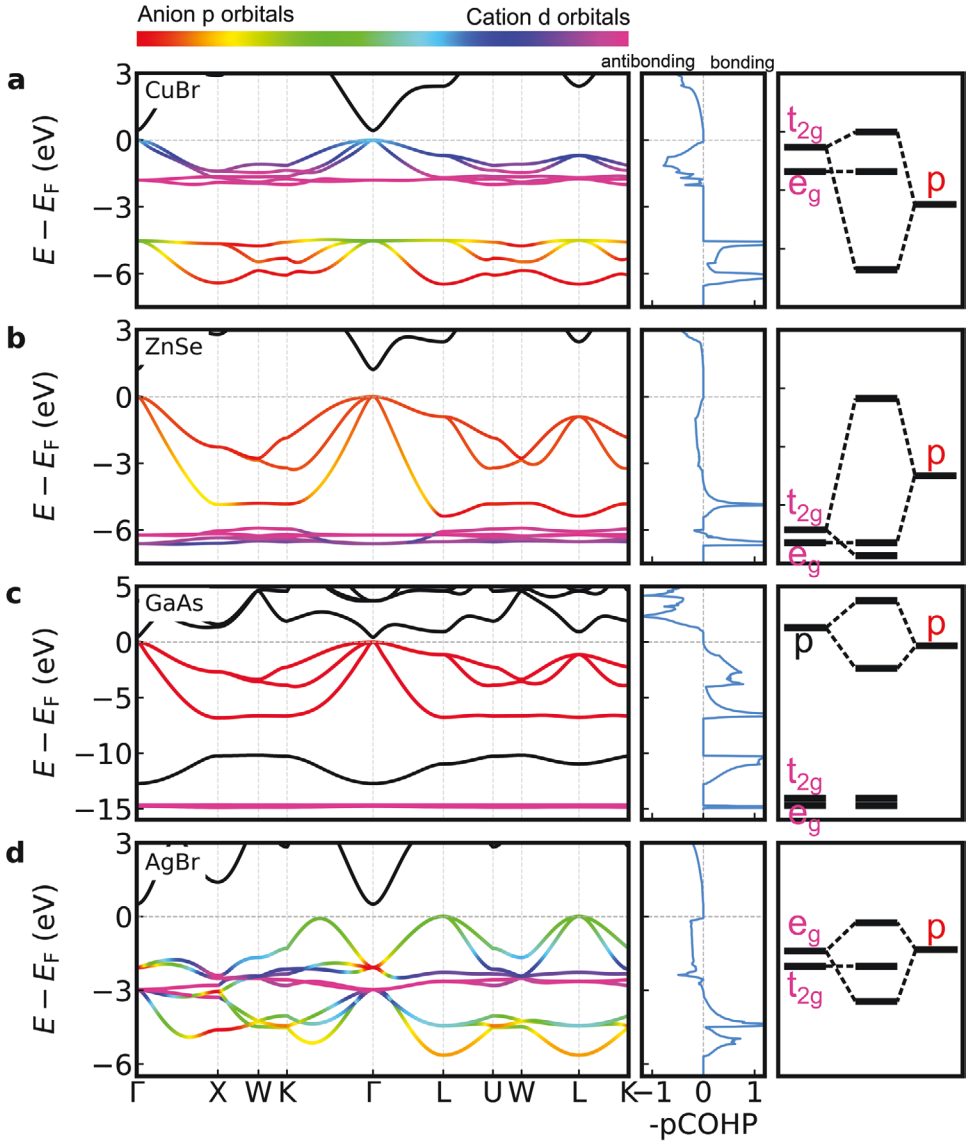

Figure 1. Orbital-projected band structures, -pCOHP, and molecular orbital diagrams of representative binary compounds. a) Zinc blende CuBr, b) zinc blende ZnSe, c) zinc blende GaAs, and d) rock-salt AgBr. Color indicates the contribution from anion *p* and cation *d* orbitals. Positive and negative -pCOHP indicate the bonding and antibonding interactions between cation and anion, respectively.

hybridization between Ga-3*d* and As-4*p* orbitals, and the valence bands consist of the hybridization between Ga-4*s* and As-4*p* orbitals only (see Figure 1c). The filled antibonding states can be explicitly seen in the COHP analysis as shown in Figure 1. The projected COHP (pCOHP) between cation *M* and anion *X* of CuBr displays a much larger antibonding peak below the Fermi level than ZnSe, while GaAs has no antibonding peak in the valence band range at all. It is worth noting that the presence of Cu-*X* antibonding states have been reported in other compounds with CuX_4 tetrahedral coordination as well, for instance, Cu_2Se[46] and Cu_2S,[47] where the effects of the antibonding states on electronic structures are pronounced.

Interestingly, we find that the strong *p-d* coupling between the filled Cu/Ag-*d* and anion *p*-orbitals exists in other polyhedra with different coordination numbers as well, such as MX_6 octahedron, MX_3 planar triangle, and MX_2 linear chain. This is because the symmetry restriction of *p-d* mixing[44,45] only holds for certain *K*-points of the first Brillouin zone. For example, the *p-d* mixing in rock-salt AgBr is only strictly prohibited at the Γ and X points where the $AgBr_6$ octahedron preserve inversion symmetry (see Figure 1d). In contrast, we can see strong *p-d* mixing at other *K*-points of the Brillouin-zone, especially along the Γ-K and Γ-L-U lines. Similar to the zinc blende CuBr, the *p-d** antibonding states are at the top of the valence bands of AgBr. Unlike CuBr, however, the valence band maximum is shifted away from the Γ point, increasing valley degeneracy. Meanwhile, since the *M-X* bond length of rock-salt is much longer than that of zinc blende, both the bonding and antibonding peaks of rock-salt are smaller than those of zinc blende, as evidenced by -pCOHP in Figure 1d. The trigonal planar and linear coordination examples are presented in Figure S1, Supporting Information. What makes Cu and Ag significantly

© 2021 Wiley-VCH GmbH

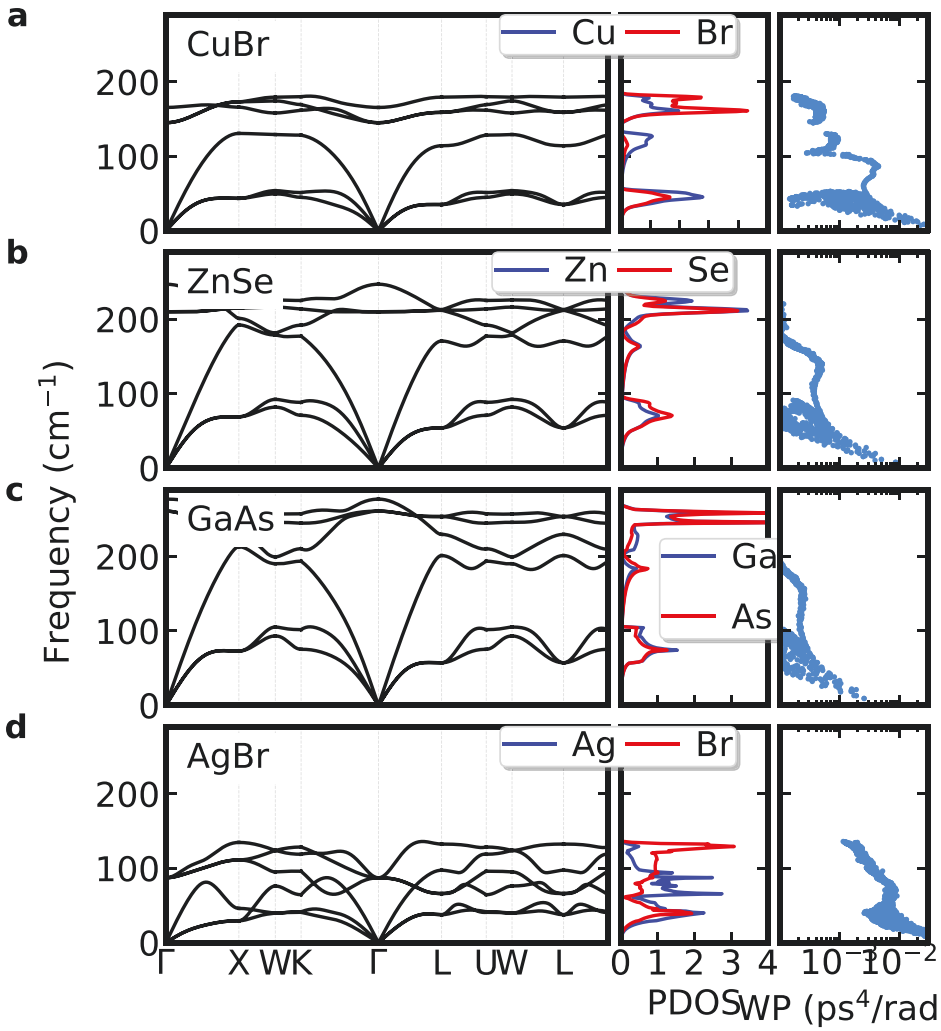

Figure 2. Phonon dispersions, phonon density of states (PDOS), and weighted phase space WP of three-phonon scattering for representative binary compounds. a) Zinc blende CuBr, b) zinc blende ZnSe, c) zinc blende GaAs, and d) rock-salt AgBr.

different from other transition metal elements such as Zn and Ga is their relatively high energy of the *d* orbitals, which essentially determines the *p-d* coupling strength since the orbitals with similar energies are more likely to interact.[44,45,47]

The occupation of the *d-p** antibonding states is expected to weaken the *M-X* bond strength, which can be quantitatively evaluated by the second-order (or harmonic) interatomic force constants (2ndIFC). Our DFT calculations show that the 2ndIFC decreases from 17.1 eV Å^{-2} in GaAs to 12.4 eV Å^{-2} in ZnSe, and to 7.2 eVÅ^{-2} in CuBr. This trend is concomitant with the dramatic decrease of the mean sound velocity (v_m, GaAs: 3.24 Km s^{-1}; ZnSe: 2.50 Km s^{-1}; CuCl: 1.90 Kms^{-1}), which is an approximation of sound group velocity (v_g).[7] As we pointed out earlier, these compounds have nearly the same $\overline{M}$, and therefore, the only reason causing a large variation in v_m is the *M-X* bond strength (*k*). Presumably, this is one of the main reasons that the κ_L of these compounds decreases significantly from GaAs to CuBr since κ_L is proportional to v_m^3.[5,25] As shown in **Figure 2**, in addition to the overall phonon softening (reduced phonon frequency) from GaAs to CuBr due to the reduced *M-X* 2ndIFC, another remarkable feature of these phonon spectra is the flattening of the two transverse acoustic (TA) branches from GaAs to CuCl. These increasingly localized (less dispersive) acoustic phonon bands significantly increase the phonon-phonon scattering rates (τ^{-1}) through providing more scattering channels, which can be quantified by the weighted phase space (WP) (i.e., three-phonon transition probability)[48] (see Figure 2). This effect has also been found in the case of an archetypal system $YbFe_4Sb_{12}$ exhibiting rattling and localized vibrations.[48] It is interesting to note from the phonon density of states in Figure 2a that the nearly flat TA modes are mainly from Cu in CuBr, even though the atomic mass of Cu is smaller than Br and the lighter atom usually appears at higher vibrational frequencies. Together with the weak bonding interaction between Cu and Br, these flat and localized vibrations suggest that Cu exhibits rattling-like behavior in the close-packed structure. We also find the optical branches are increasingly softened around the Γ point from GaAs to CuBr. This softening is commonly seen in the rock-salt compounds such as SnTe and PbTe,[49] which has been partially attributed to the cause of low κ_L, but it is not common in zinc blende systems.[19,31] As discussed above, the bond softening mechanism is not limited to zinc blende

© 2021 Wiley-VCH GmbH

structure. All these features observed in the zinc blende structure also appear in rock-salt AgBr ($\kappa_L = 1.1\ Wm^{-1}\ K^{-1}$ at 300 K[50]), and since the *M*-*X* bond length in the rock-salt structure is usually longer, AgBr has much softer phonon frequencies, lower v_m, larger WP, thus low κ_L. With the above analysis and discussion in mind, we can conclude that antibonding from this unusual *p*-*d* hybridization in Cu/Ag-based compounds can be leveraged to effectively weaken interatomic interactions, which serves as our first design strategy for the discovery of materials with intrinsically low κ_L.

2.2. Design Strategy II: Edge and Face-Sharing Polyhedra

In addition to forming the antibonding states, an alternative strategy to weaken the *M*-*X* bond and hence to have lower κ_L is to have higher CN.[24,25] However, Cu^+ and Ag^+ are generally too small to sit in the polyhedron with CN $\geqslant$ 6. In this case, according to Pauling's third rule,[22] the *M*-*X* bond strength can be further weakened provided the MX_4 tetrahedra (or more generally MX_n polyhedra, *n* is the CN) are edge or even face-sharing. This is due to the following two effects: i) the distance between two *M* cations is significantly reduced in the edge and face-sharing polyhedron compared to that in the corner-sharing one, and ii) the resulting Coulomb repulsion among *M* cations is so strong that the *M*-*X* bond has to be elongated to increase the *M*-*M* distance and therefore to alleviate Coulomb repulsion. Apparently, the *M*-*X* bond elongation is much larger in polyhedra with low CN than those with high CN because the *M*-*M* distance is shorter in the former (Pauling's second rule[22]). Therefore, this strategy is more effective for tetrahedron, which is the main focus of this work. Note that although cations with a higher oxidation state have larger Coulomb repulsion, only Cu^+ and Ag^+ are considered in this work because we want to take advantage of the *M*-*X* antibonding originating from *p*-*d* coupling. Furthermore, both Cu^+ and Ag^+ tend to form low-coordination polyhedra, such as tetrahedra and trigonal planars with chalcogens and halogens. These anions (except fluorine) are highly polarizable and widely used in thermoelectric materials.[51]

It is worth noting that although many Cu-based compounds have been intensively optimized for thermoelectric applications,[34,36–43] most of these studies focus on the diamond-like structures, for example, chalcopyrite, famatinite, and stannite, which only contain the corner-sharing CuX_4 tetrahedra and are certainly not ideal thermoelectric materials in terms of κ_L based on our analysis (e.g., the κ_L of $CuFeS_2$, $CuFeSe_2$, $CuGaTe_2$, Cu_3SbS_4, and $Cu_2ZnSnSe_4$ at 300 K are 7.8, 6.5, 6.4, 3.5, and 3.2 $Wm^{-1}\ K^{-1}$, respectively[24,52,53]). To illustrate this, in **Figure 3**, we compare the *M*-Se bond lengths and 2ndIFCs of Cu/Se and Ag/Se compounds with chalcopyrite and ZrCuSiAs-type structures. In contrast to the corner-sharing tetrahedra in chalcopyrite, the ZrCuSiAs-type structure features a layered structure with edge-sharing $CuAs_4$ tetrahedra within the layer (see **Figure 4**). It is clear that the ZrCuSiAs-type compounds (BiCuSeO, LaCuSeO, BaCuSeF, SrCuSeF, BiAgSeO, BaAgSeF, and SrAgSeF) have longer *M*-Se bond lengths and smaller 2ndIFCs than those of chalcopyrite compounds ($CuAlSe_2$, $CuGaSe_2$, $CuInSe_2$, $CuTlSe_2$, $AgAlSe_2$, $AgGaSe_2$, and $AgInSe_2$).

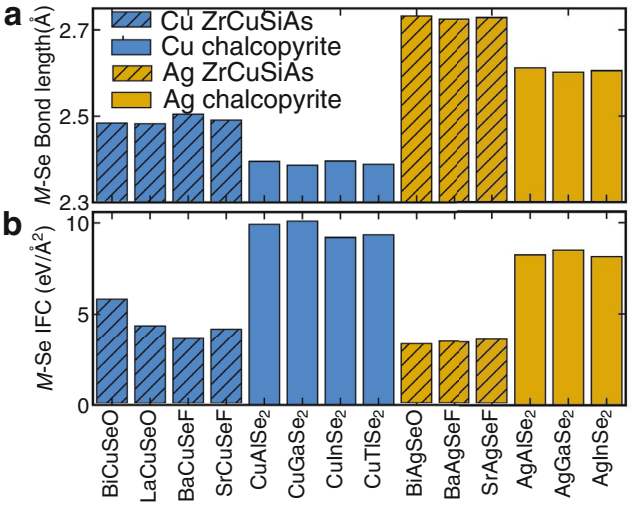

Figure 3. Bond lengths and force constants of Cu/Ag compounds with chalcopyrite and ZrCuSiAs-type structures. a) *M*-Se (*M* =Cu and Ag) bond lengths. b) 2nd order interatomic force constants between *M* and Se. Blue and yellow balls are Cu^+ and Ag^+ compounds, respectively.

This is also consistent with the fact that ZrCuSiAs-type compounds have lower κ_L than chalcopyrite (see Table S1, Supporting Information). Another set of examples is Cu_2X (*X* = S, Se, and Te), which adopts the antifluorite structure at elevated temperatures, wherein the CuX_4 tetrahedra are edge-sharing in a three-dimensional (3D) network. These compounds are well-studied as thermoelectric materials due to the low κ_L.[39,54,55] In these high-temperature phases, Cu^+ ions do not stay at the centers of CuX_4 tetrahedra (the ideal position of the antifluorite structure) but hop around the center and therefore exhibit superionic behavior.[56,57] This facile ionic hopping is ultimately due to the weak Cu-*X* bond, as the consequence of both the filled *p*-*d** antibonding states and the 3D edge-sharing CuX_4 tetrahedra. In the 3D case, since the CuX_4 tetrahedra are edge-sharing through all Cu-*X* edges, the strong Coulomb repulsion between Cu^+ cations is available in all three dimensions. Consequently, the Cu-*X* bond is further weakened compared to the layered (2D) edge-sharing CuX_4 tetrahedra, which is likely the main reason why Cu^+ migration occurs in Cu_2X but not in the ZrCuSiAs-type structure. Therefore, edge/face-sharing MX_n polyhedra serves as our second design strategy for the discovery of materials with intrinsically low κ_L.

2.3. Screening Existing Compounds from ICSD

We next apply these two design rules to search for novel, low κ_L compounds. We search for the experimentally synthesized compounds that have an edge or face-sharing MX_n (M = Cu^+ and Ag^+; X = S, Se, Te, Cl, Br, and I; $n < 6$) polyhedra from the inorganic crystal structure database (ICSD)[58] using the coordination environments analysis tool developed in the Materials Project.[59,60] We find 70 compounds in 21 prototype structures, as summarized in **Table 1** and Table S2, Supporting Information. We calculated zero-kelvin phonon spectra of all these compounds and found 27 of them have small imaginary frequencies,

© 2021 Wiley-VCH GmbH

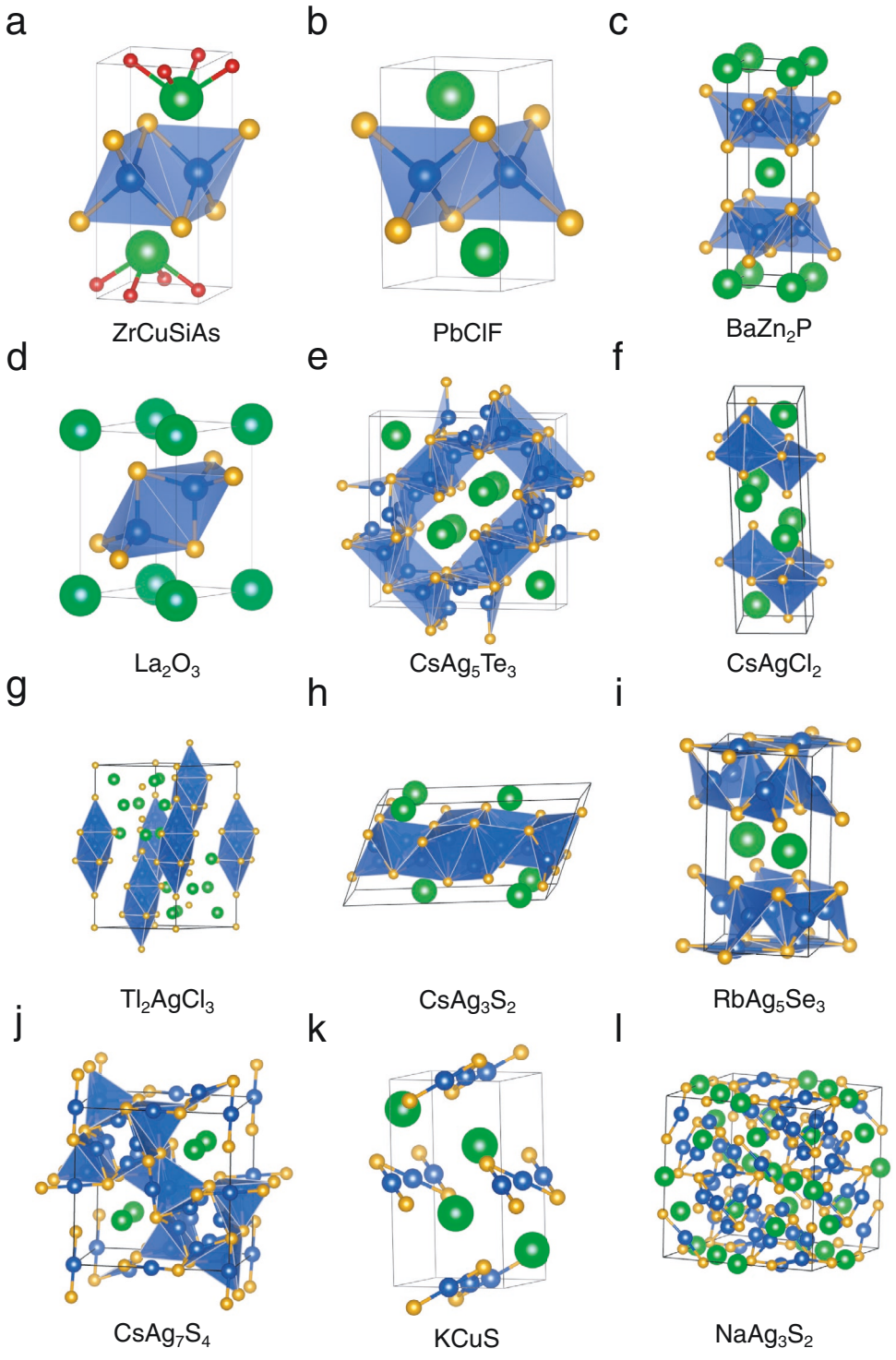

Figure 4. Prototype structures with different MX_n polyhedra. a) ZrCuSiAs ($P4/nmm$), b) PbClF ($P4/nmm$), c) $BaZn_2P_2$ ($I4/mmm$), d) La_2O_3 ($P\bar{3}m1$), e) $CsAg_5Te_3$ ($P4_2/mnm$), f) $CsAgCl_2$ ($Cmcm$), g) Tl_2AgCl_3 ($R\bar{3}$), h) $CsAg_3S_2$ ($C2/m$), i) $RbAg_5Se_3$ ($P4/nbm$), j) $CsAg_7S_4$ ($P4/n$), k) KCuS ($Pna2_1$), and l) $NaAg_3S_2$ ($Fd\bar{3}m$). Blue, green, orange, and red spheres represent Cu/Ag, alkali/alkaline-earth metal, chalcogens/(Cl, Br, I), and O/F atoms, respectively.

which means these compounds only crystallize in their reported structures at measured temperatures, for example, room temperature. Additional calculations of phonon renormalization at room temperature are needed to stabilize these imaginary frequencies and compute their κ_L. Owing to the high computational cost of phonon renormalization for such a large set of compounds,[61] we only calculated κ_L of all the compounds that have no imaginary frequency at 0 K. The compounds with

© 2021 Wiley-VCH GmbH

Table 1. The properties of our calculated compounds discovered from the ICSD using our screening strategy. Prototype structure, space group, number of atoms per primitive cell (N), average atom mass (amu.), the shortest M-M distance between two MX_n polyhedra (d^{M-M}, Å), mean sound velocity (v_m), and diagonal terms of κ_L (κ_L^{xx}, κ_L^{yy}, κ_L^{zz}) at 300 K of the calculated compounds. The way of polyhedra (octahedra, OC; tetrahedra, TE; trigona, TR; trigonal bipyramids, TB; square planars, SP; linear chains: LN) sharing with others through corner (·), edge (-), or face (|) is indicated as polyhedra sharing style. The κ_L values including the off-diagonal terms of heat current operator[65] are in bold.

Compound	Structure	Polyhedra sharing style	Space group	N	$\overline{M}$	d^{M-M} (Å)	v_m (m/s)	κ_L^{xx}, κ_L^{yy}, κ_L^{zz} ($WK^{-1}m^{-1}$)
SmCuSeO	ZrCuSiAs	TE-TE	$P4/nmm$	8	77.22	2.769	2561	4.16, 4.16, 0.90
EuCuSeO	ZrCuSiAs	TE-TE	$P4/nmm$	8	77.62	2.754	2541	3.29, 3.29, 0.53
GdCuSeO	ZrCuSiAs	TE-TE	$P4/nmm$	8	78.94	2.739	2693	3.69, 3.69, 0.81
DyCuSeO	ZrCuSiAs	TE-TE	$P4/nmm$	8	80.25	2.713	2524	3.27, 3.27, 0.57
BiAgSeO	ZrCuSiAs	TE-TE	$P4/nmm$	8	102.95	2.806	2245	1.28, 1.28, 0.22
SrCuSF	ZrCuSiAs	TE-TE	$P4/nmm$	8	50.56	2.761	3071	3.17, 3.17, 1.81
BaCuSF	ZrCuSiAs	TE-TE	$P4/nmm$	8	62.99	2.868	2675	1.95, 1.95, 1.84
SrAgSF	ZrCuSiAs	TE-TE	$P4/nmm$	8	61.64	2.857	2698	1.73, 1.73, 0.45
BaAgSF	ZrCuSiAs	TE-TE	$P4/nmm$	8	74.07	2.977	2428	1.92, 1.92, 0.97
SrCuSeF	ZrCuSiAs	TE-TE	$P4/nmm$	8	62.28	2.845	2552	1.79, 1.79, 0.62
SrAgSeF	ZrCuSiAs	TE-TE	$P4/nmm$	8	73.36	2.924	2400	1.67, 1.67, 0.66
BaAgSeF	ZrCuSiAs	TE-TE	$P4/nmm$	8	85.79	3.056	2199	1.55, 1.55, 0.85
SrAgTeF	ZrCuSiAs	TE-TE	$P4/nmm$	8	85.52	3.039	2130	0.97, 0.97, 0.61
BaAgTeF	ZrCuSiAs	TE-TE	$P4/nmm$	8	97.95	3.189	1775	0.90, 0.90, 0.30
PbCuSeF	ZrCuSiAs	TE-TE	$P4/nmm$	8	92.18	2.827	1842	0.80, 0.80, 0.44
PbAgSeF	ZrCuSiAs	TE-TE	$P4/nmm$	8	103.26	2.892	1914	0.83, 0.83, 0.53
PbAgTeF	ZrCuSiAs	TE-TE	$P4/nmm$	8	174.11	2.982	1770	0.58, 0.58, 0.32
NaCuSe	PbClF	TE-TE	$I4/nmm$	6	55.17	2.848	2383	0.68, 0.68, 0.51
NaAgSe	PbClF	TE-TE	$P4/nmm$	6	69.94	2.969	2038	0.74, 0.74, 0.61
KAgSe	PbClF	TE-TE	$I4/nmm$	6	75.31	3.141	1932	0.67, 0.67, 0.47
$CaCu_2S_2$	La_2O_3	TE-TE	$P\bar{3}m1$	5	46.26	2.765	3206	2.20, 2.20, 1.51
$BaAg_2S_2$	La_2O_3	TE-TE	$P\bar{3}m1$	5	83.44	3.086	1943	1.06, 1.06, 0.64
$TlAgI_2$	InTe-Tl_2Se_2	TE-TE	$I4/mcm$	8	141.51	3.780	1276	0.14, 0.14, 0.15
$CsCu_2ICl_2$	$CsCu_2ICl_2$	TE-TE	$P2_1/m$	12	76.30	2.620	1238	**0.15**, **0.23**, **0.16**
$AgSbTe_2$	$NaFeO_2$	OC-OC	$R\bar{3}m$	4	121.20	4.278	1847	1.34, 1.34, 0.95
$CsAgCl_2$	$CsAgCl_2$	TB-TB	$Cmcm$	8	77.92	4.005	1350	0.13, 0.07, 0.17
$TlCu_5Se_3$	$CsAg_5Te_3$	TE-TE, TE-TR	$P4_2/mnm$	36	84.33	2.535	1842	0.19, 0.19, 0.34
$CsAg_5Se_3$	$CsAg_5Te_3$	TE-TE, TE-TR	$P4_2/mnm$	36	101.02	2.838	1661	**0.20**, **0.20**, **0.27**
Tl_2AgCl_3	Tl_2AgCl_3	TE|OC	$R\bar{3}$	18	103.83	2.996	1252	**0.24**, **0.24**, **0.24**
Tl_2AgBr_3	Tl_2AgCl_3	TE|OC	$R\bar{3}$	18	126.06	3.004	1176	**0.16**, **0.16**, **0.18**
Tl_2AgI_3	Tl_2AgCl_3	TE|OC	$R\bar{3}$	18	149.56	2.998	1151	**0.13**, **0.13**, **0.17**
KCu_3S_2	$CsAg_3S_2$	TE-TE, TE|TE, TE-TR	$C2/m$	12	48.98	2.563	2455	0.75, 0.61, 0.72
$RbCu_3S_2$	$CsAg_3S_2$	TE-TE, TE|TE, TE-TR	$C2/m$	12	56.71	2.576	2363	0.46, 0.52, 0.50
$RbAg_3S_2$	$CsAg_3S_2$	TE-TE, TE|TE, TE-TR	$C2/m$	12	78.87	2.845	1823	0.15, 0.21, 0.14
$RbAg_3Se_2$	$CsAg_3S_2$	TE-TE, TE|TE, TE-TR	$C2/m$	12	94.50	2.849	1702	**0.29**, **0.30**, **0.16**
$CsAg_3S_2$	$CsAg_3S_2$	TE-TE, TE|TE, TE-TR	$C2/m$	12	86.78	2.855	1759	0.18, 0.26, 0.17
$CsAg_3Se_2$	$CsAg_3S_2$	TE-TE, TE|TE, TE-TR	$C2/m$	12	102.41	2.844	1672	0.08, 0.10, 0.11
KAg_3Se_2	$CsAg_3S_2$	TE-TE, TE|TE, TE-TR	$C2/m$	12	86.77	2.849	1700	0.11, 0.12, 0.19
$BaCu_2Te_2$	$BaCu_2S_2$	TE-TE, TE·TE	$Pnma$	20	103.92	2.837	2040	0.58, 1.23, 0.69
AgTlSe	TiNiSi	TE-TE, TE·TE	$Pnma$	12	130.40	3.887	1406	0.29, 0.46, 0.41
$RbAg_5Se_3$	$RbAg_5Se_3$	SP-SP, TR·TR	$P4/nbm$	18	95.74	2.997	1555	0.20, 0.20, 0.10
Ag_5SbSe_4	Ag_5SbS_4	TE-TE, TE|TE, TE·TE, TE·TR	$Cmc2_1$	20	97.70	2.831	1497	**0.26**, **0.23**, **0.20**
$TlCu_7S_4$	$CsAg_7S_4$	TE-TE, TE-TR, TE·LN, TR·LN	$P4/n$	48	64.79	2.567	2137	**0.29**, **0.29**, **0.45**
$RbAg_7S_4$	$CsAg_7S_4$	TE-TE, TE-TR, TE·LN, TR·LN	$P4/n$	48	80.74	2.908	1785	**0.15**, **0.15**, **0.26**
$CsAg_7S_4$	$CsAg_7S_4$	TE-TE, TE-TR, TE·LN, TR·LN	$P4/n$	48	84.69	2.838	1756	**0.23**, **0.23**, **0.39**
KCuS	KCuS	LN·LN	$Pna2_1$	12	44.90	2.606	1579	1.34, 1.34, 3.12

© 2021 Wiley-VCH GmbH

imaginary frequency are collected in Table S2, Supporting Information. As shown in Figure 4, the corresponding structure types can be classified in the following five categories:

i. Edge-sharing polyhedra, including ZrCuSiAs, PbClF, $BaZn_2P_2$, La_2O_3, $CsCu_2ICl_2$, $SrCuBiOSe_2$, InTe-Tl_2Se_2, $CsAg_5Te_3$, $CsAgCl_2$, $NaFeO_2$, and Ag_5SbSe_4-type structures.
ii. Face-sharing polyhedra, including Tl_2AgCl_3-type structure.
iii. Coexistence of edge-sharing and face-sharing polyhedra, including $CsAg_3S_2$-type structure.
iv. Coexistence of edge-sharing and corner-sharing polyhedra, including $RbAg_5Se_3$, β-$BaCu_2S_2$, TiNiSi, and $CsAg_7S_4$-type structures.
v. Corner-sharing linear chain, including KCuS and Ti_2Ni-type structures.

2.3.1. Edge-Sharing Polyhedra

As mentioned above, MX_4 tetrahedra are edge-sharing with each other within the layer perpendicular to the *c*-axis in the ZrCuSiAs-type structure, see Figure 4a. The well-studied thermoelectric material having this structure type is BiCuSeO, which has κ_L of ≈ 1 Wm^{-1} K^{-1} at 300 K.[34,38] The low κ_L of BiCuSeO was initially attributed to the strong anharmonicity caused by the lone-pair electrons cation Bi^{3+}.[62] However, more recent studies suggest that the low-frequency rattling-like phonon modes coming from Cu^+ play more important roles in suppressing its thermal transport.[63,64] This proposal is supported by the large atomic displacement parameter (ADP) of Cu^+ cation.[63] The large ADP of Cu is due to the weak Cu-Se bond, which originates from the antibonding *p*-*d** states and the edge-sharing tetrahedra. Our local coordination environment search identifies 20 other Cu and Ag-based ZrCuSiAs-type compounds, and 16 of them have no imaginary frequency. Our elastic constant and anharmonic phonon calculations show that all of them have relatively low v_m and κ_L in terms of their $\overline{M}$, even though many of them do not have lone-pair electrons cations and all of them contain strong ionic bond *A*-O/F (*A* is another metal element) (see Table 1).

The PbClF-type structure is the ZrCuSiAs-type one with an anion or cation vacancy, and we only focus on the anion vacancy case (see Figure 4b). Only two Cu and one Ag compounds are reported in the ICSD, and our calculations show that NaCuTe has imaginary frequencies (see Table S2, Supporting Information), and both NaCuSe and KAgSe have very low κ_L at 300 K. We note the κ_L of these two compounds are lower than many ZrCuSiAs-type compounds with similar $\overline{M}$. Presumably, this is because the other cation (e.g., Na and K) is also less bonded, further weakening the bonding interactions within these compounds. For example, the 2ndIFC between Na and Se in NaCuSe is 2.05 eV $Å^{-2}$, whereas the 2ndIFC between La and O in LaCuSeO is 7.36 eV $Å^{-2}$. This can be further verified by monitoring the difference of v_m between these two structures. For example, although KAgSe has a similar $\overline{M}$ (≈74 aum.) to SrAgSeF, the v_m of KAgSe (1993 m s^{-1}) is much smaller than that of SrAgSeF (2415 m s^{-1}).

The $BaZn_2P_2$-type structure has two edge-sharing MX_4 tetrahedra layers separated by a Ba^{2+} layer (see Figure 4c), which is similar to the PbClF-type structure. The β phase of $BaCu_2S_2$ and $BaCu_2Se_2$ are the only atom-ordered Cu^+/Ag^+ compounds (i.e., without partial occupancy) reported in the ICSD. Their κ_L have been studied experimentally.[33,66] Our calculated κ_L of these two compounds are ≈2.08 and 0.87 Wm^{-1} K^{-1} (see Table S1, Supporting Information), which are slightly higher than the experimental values. Note that our calculated κ_L are possibly overestimated for many of these compounds because our calculations do not include the higher-order phonon-phonon scattering, phonon softening due to lattice thermal expansion, and defects and grain boundary scattering. The low κ_L of the compounds that do not contain lone-pair electrons cations highlight the key structural character of suppressing heat transfer from the edge-sharing CuX_4 tetrahedra.

Other structures that only contain edge-sharing MX_4 tetrahedra are La_2O_3 ($CaCu_2S_2$ and $BaAg_2S_2$, see Figure 4d), InTe-Tl_2Se_2 ($TlAgI_2$), $CsCu_2ICl_2$ ($CsCu_2ICl_2$), and $SrCuBiOSe_2$-type ($SrCuBiOSe_2$) structures (see Table 1 and Table S1, Supporting Information). Both $CaCu_2S_2$ and $BaAg_2S_2$ have very low κ_L despite their small unit cell, light $\overline{M}$, and high symmetry. The other three compounds have relatively larger unit cell and low symmetry. They all have very low κ_L. The κ_L of $SrCuBiOSe_2$ has been studied experimentally recently,[67] which agrees well with our calculated value (see Table S1, Supporting Information).

The $CsAg_5Te_3$-type structure contains edge-sharing $AgTe_4$ tetrahedra and edge-sharing polyhedra between $AgTe_4$ tetrahedra and $AgTe_3$ pyramids (Figure 4e). The distance between the Ag cations in two edge-sharing tetrahedra is 3.1 Å and that between tetrahedron and pyramid is 2.9 Å. Since this structure has a relatively high symmetry (space group $P4_2/mnm$), the complex local coordination leads to a large unit cell (36 atoms per primitive cell). Three compounds ($TlCu_5Se_3$, $CsAg_5Se_3$, and $CsAg_5Te_3$) are found in this structure type and all have low v_m and ultralow κ_L, (see Table 1 and Table S1, Supporting Information). Experimentally, $CsAg_5Te_3$ is found to exhibit ultralow κ_L (0.18 Wm^{-1} K^{-1}) at room temperature.[17] Our calculated κ_L (0.05 Wm^{-1} K^{-1}) without off-diagonal terms of heat current operator is much lower than the experimental value, indicating the possible breakdown of the phonon gas model,[68] which is evidenced by the glasslike and nearly temperature-independent κ_L observed in the experiment.[17] An excellent agreement with the experiment is achieved once the off-diagonal terms are included in our calculations[65] (see Table S1, Supporting Information).

$CsAgCl_2$ is the only structure that has the edge-sharing trigonal bipyramidal $AgCl_5$ (see Figure 4f). Since one Ag^+ coordinates with five Cl^-, the distance between Ag^+ cations in two trigonal bipyramid (4.0 Å) is larger than that in the edge-sharing tetrahedron (≈3.0 Å) but smaller than the edge-sharing octahedron (4.3 Å) (see Table 1). The small $\overline{M}$ (78 amu.) but low v_m (≈1200 m s^{-1}) indicate the weak bonding interaction within the compound. Even though the unit cell is relatively small (8 atoms per primitive unit cell), such low v_m still leads to an ultralow κ_L (≈0.1 Wm^{-1} K^{-1}) (see Table 1).

$NaFeO_2$-type $AgSbTe_2$ is the only compound that has edge-sharing octahedra. In the hexagonal structure ($R\bar{3}m$ space group), $AgTe_6$ octahedra are edge-sharing and form a layer that is separated by the $SbTe_6$ octahedral layer. In a $AgTe_6$ octahedron, the Ag-Te bond (2.931 Å) is much longer than that in the tetrahedral coordination, such as $AgInTe_2$ (2.743 Å). The weak bond makes $AgSbTe_2$ have a relatively lower v_m (1885 m s^{-1}) and κ_L

© 2021 Wiley-VCH GmbH

(1.21 Wm^{-1} K^{-1}) than PbTe (v_m = 2206 m s^{-1}; κ_L = 2.5 Wm^{-1} K^{-1}), which is also octahedrally coordinated and has larger $\overline{M}$.

Ag_5SbSe_4 is a unique structure that contains face-sharing tetrahedra, corner-sharing tetrahedra, and corner-sharing polyhedra between tetrahedra and trigonal planars, which leads to a highly distorted structure with 20 atoms per primitive unit cell. The shortest Ag-Ag distance is from two corner-sharing tetrahedra (2.8 Å), which is very unusual. Besides, the face-sharing tetrahedra also lead to short Ag-Ag distance (3.0 Å). Therefore, the v_m and κ_L are quite small in terms of $\overline{M}$ and unit cell size.

2.3.2. Face-Sharing Polyhedra

As indicated by our design strategy II, face-sharing polyhedra are even more highly desired to lower κ_L. The Tl_2AgCl_3-type structure has a $AgCl_6$ octahedron face-sharing with two $AgCl_4$ tetrahedra at two opposite faces (Figure 4g). The Ag-Ag distance between the Ag in tetrahedra and the Ag in octahedra is only about 3.0 Å, showing a strong Coulomb repulsion. However, the face-sharing polyhedra do not connect with others, limiting the effect of bond weakening by face-sharing. All the three reported compounds (Tl_2AgCl_3, Tl_2AgBr_3, and Tl_2AgI_3) contain the heavy element Tl and very ionic halogen elements. Therefore, these compounds have very low v_m (≈1200 m s^{-1}) and κ_L from our calculations. Similar to the compounds with $CsAg_5Te_3$-type structure, the calculated κ_L without off-diagonal terms of heat current operator are largely underestimated since the conventional phonon picture breaks down here,[69] which more likely happens in compounds with ultralow κ_L.

2.3.3. Coexistence of Edge-Sharing and Face-Sharing Polyhedra

$CsAg_3S_2$-type structure has quite low symmetry (space group $C2/m$) due to the complex local coordination: edge-sharing AgS_4 tetrahedra, face-sharing AgS_4 tetrahedra, and edge-sharing polyhedra between AgS_4 tetrahedra and AgS_3 trigonal pyramids (see Figure 4h). The shortest distance between Ag^+ cations in two face-sharing tetrahedra is only 2.84 Å. In addition to the short Ag-Ag distance between two edge-sharing AgS_4 tetrahedra, the Ag^+ cation in the trigonal planars suffers from the Coulomb repulsion from the Ag^+ cations in two AgS_4 tetrahedra (Ag^+-Ag^+ distance is just 2.98 Å, which is much smaller than that of 3.85 Å in chalcopyrite $AgGaS_2$). Therefore, all 7 dynamically stable compounds (5 compounds have imaginary frequencies, see Table S2, Supporting Information) of this structure have relatively low v_m and κ_L although they have small $\overline{M}$ and fewer atoms in the primitive unit cell.

2.3.4. Coexistence of Edge-Sharing and Corner-Sharing Polyhedra

$RbAg_5Se_3$-type structure has a unique layered structure consisting of corner-sharing trigonal pyramids $AgSe_3$ and edge-sharing square planars $AgSe_4$ (see Figure 4i). Four $AgSe_3$ trigonal pyramids share with a Se^{2-} corner in a layer. Four Ag^+ cations in four square planars share a Se^{2-} in another layer and every two of them share a Se-Se edge. Therefore, Ag and Se form a layer. Two Ag-Se layers are separated by a Rb layer. The Ag-Ag distances between two trigonal pyramids and two square planars are 3.0 and 4.2 Å, respectively. The short distance of two Ag^+ cations elongates the Ag-Se bond lengths. Therefore, the moderate $\overline{M}$ (95.7 amu.) can lead to relatively low v_m (1531 m/s) and low κ_L (≈0.2 Wm^{-1} K^{-1}) (see Table 1).

Different from the β-$BaCu_2S_2$ ($BaZn_2P_2$-type structure), α-$BaCu_2S_2$ has both corner-sharing and edge-sharing $CuSe_4$ tetrahedra and lower symmetry (space group *Pnma*). Since the corner-sharing polyhedra do not provide bond softening as that of edge/face-sharing polyhedra (design strategy II), the α-$BaCu_2S_2$ has higher κ_L (≈1.5 Wm^{-1} K^{-1}) than β-$BaCu_2S_2$ experimentally.[70] $BaCu_2Te_2$ also crystallizes in the α-$BaCu_2S_2$-type structure and our calculations show it has a relatively low κ_L, mainly benefiting from the heavier and lower electronegativity Te.

The $CsAg_7S_4$-type structure has relatively high symmetry (space group $P4/n$) but a large number of atoms in a primitive unit cell (see Figure 4j). It has AgS_4 tetrahedra, AgS_3 trigonal planars, and S-Ag-S linear chains. Edge-sharing polyhedra exist between two AgS_4 tetrahedra and between AgS_4 tetrahedron and AgS_3 trigonal planars. Also, there are corner-sharing polyhedra between AgS_4 tetrahedron and AgS_3 trigonal planar, between AgS_4 tetrahedron and S-Ag-S linear chain, and between AgS_3 trigonal planars and S-Ag-S linear chain. The shortest Ag-Ag distance (2.83 Å) is between two edge-sharing tetrahedra. Three compounds are reported in the ICSD, and all are dynamically stable at 0 K. Although these compounds have relatively low $\overline{M}$, the weak *M*-*X* bond and complex structure lead to low v_m and κ_L.

Both AgTlSe and AgTlTe crystallize in the TiNiSi-type structure, where $AgSe_4$ tetrahedra are edge and corner-sharing with other tetrahedra. Since the $AgSe_4$ tetrahedra are slightly distorted, the Ag-Ag distance between two edge-sharing tetrahedra is larger than many cases with edge-sharing tetrahedra. However, the short Tl^+-Ag^+ distance (3.28 Å) could provide extra Coulomb repulsion to weaken Ag-*X* and Tl-*X* bonds. Weak Ag-*X* bonds together with a large $\overline{M}$ originating from Tl and Te result in slow v_m and low κ_L. Our calculated κ_L is slightly lower than the experimental value (0.43 Wm^{-1} K^{-1})[71] (see Table S1, Supporting Information).

2.3.5. Corner-Sharing Linear Chain

The only way to increase *M*-*M* Coulomb repulsion in the *X*-*M*-*X* linear chain is to form nonlinear corner-sharing chains. The KCuS-type structure has S-Cu-S zigzag chains along the *c*-axis (see Figure 4k). Therefore, the shortest Cu-Cu distance in the KCuS structure is reduced to 2.61 Å. The Cu-S bond length in KCuS is around 2.134 Å. Although KCuS has a very small $\overline{M}$ (≈45 amu.) and relatively small unit cell (12 atoms per primitive cell), it has low v_m and κ_L, mainly due to the weak Cu-S bond and the hollow structure.

Another interesting structure is the Ti_2Ni-type structure (see Figure 4l). $NaAg_3S_2$ and KAg_3S_2 adopt this structure. In these compounds, six S-Ag-S linear chains form a tetrahedral cluster, where very three S-Ag-S linear chains share a S^{2-} corner. Our phonon calculations show many imaginary frequencies in these two compounds, and the very localized unstable phonon

© 2021 Wiley-VCH GmbH

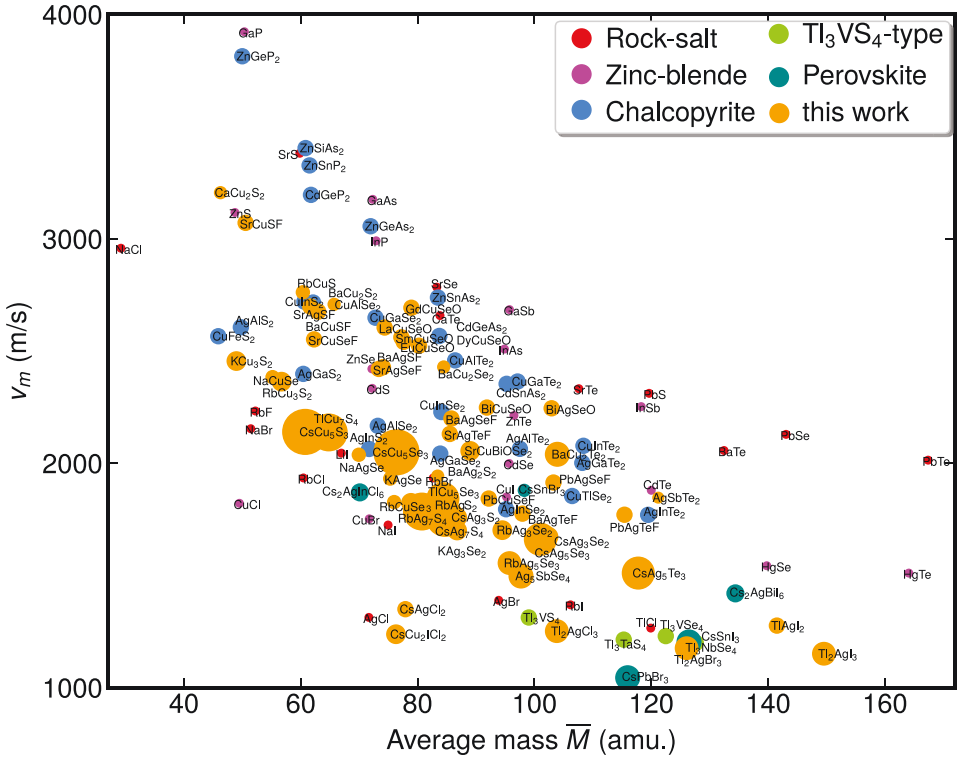

Figure 5. Dependence of v_m on $\overline{M}$ for compounds with typical structures and the compounds discovered in this work. The size of the dot is proportional to the number of atoms per primitive cell.

modes are mainly from the Ag^+ cation, originating from the weak Ag-S bond.

3. Discussion

All the compounds that we discovered in this work, whose κ_L have been experimentally measured in previous works, are tabulated in Table S1, Supporting Information. Our calculated κ_L compare well with the experimental values, which indicates that our method used in κ_L calculation is reliable. Note that the underestimation and overestimation may occur in the compounds with relatively high and ultralow κ_L, respectively, due to the omission of high-order phonon-phonon scattering, off-diagonal terms of the heat current operator, other scattering mechanisms (e.g., defect and grain boundary, etc.), and the effects of temperature on the phonon spectrum (phonon renormalization).[61,69,72] Since the phonon renormalization calculation is too expensive for such a large amount of compounds with complex structures, we only included the off-diagonal term for those compounds with calculated κ_L less than 0.1 Wm^{-1} K^{-1} when the off-diagonal terms are ignored.

To further illustrate the weak *M*-*X* bonds of the compounds discovered based on our design strategies, we compare their bond strength *K* with other compounds that have different crystal structures. Since the speed of acoustic phonon modes propagating through lattices is characterized by v_m, which is proportional to $\sqrt{K/M}$,[4] we plot the computed v_m using elastic constants as a function of average mass $\overline{M}$ in **Figure 5**. As expected, we observe an overall decrease of v_m with increasing $\overline{M}$. As we mentioned before, the rock-salt structure has a longer cation-anion bond length and, therefore, smaller *K* than zinc blende. This is indeed what we observed in Figure 5: rock-salt generally has lower v_m than zinc blende. Meanwhile, *K* can also be affected by types of chemical bonds, for example, ionic bond or covalent bond. We can see from Figure 5 that both rock-salt and zinc blende compounds can be categorized into two groups: i) high v_m group, which mainly includes the IIA-VIA and IVA-VIA rock-salt, and IIB-VIA and IIIA-VA zinc blende; ii) low v_m group, which is mainly composed of the IA-VIIA and IB-VIIA compounds. The presence of *M*-*X* anti-bonding states is the main cause of the small *K* in these IB-VIIA compounds, which are less ionic. The effects of the *p*-*d* hybridization on chalcopyrite compounds can also be clearly seen in the much-reduced v_m for the compounds containing Cu/Ag. Overall, we see that the compounds contain Cu^+ and Ag^+ have much lower v_m than the other compounds with similar $\overline{M}$. However, such an effect is less remarkable than these in the rock-salt and zinc blende because the bond between *X* with another cation affects the *K* as well. It is thus conclusive that all the compounds we discovered have relatively lower v_m than the other compounds with similar $\overline{M}$ but don't satisfy our design strategy. Some of them even have comparable v_m with the low-v_m groups, for example, halide perovskites and Tl_3VS_4-type compounds, known as the materials with ultralow κ_L.[24,69,73,74]

In addition to lowering v_m, weak bond usually lead to stronger anharmonicity and higher phonon-phonon scattering rate (τ^{-1}) as well. In **Figure 6**a, we show three-phonon scattering

© 2021 Wiley-VCH GmbH

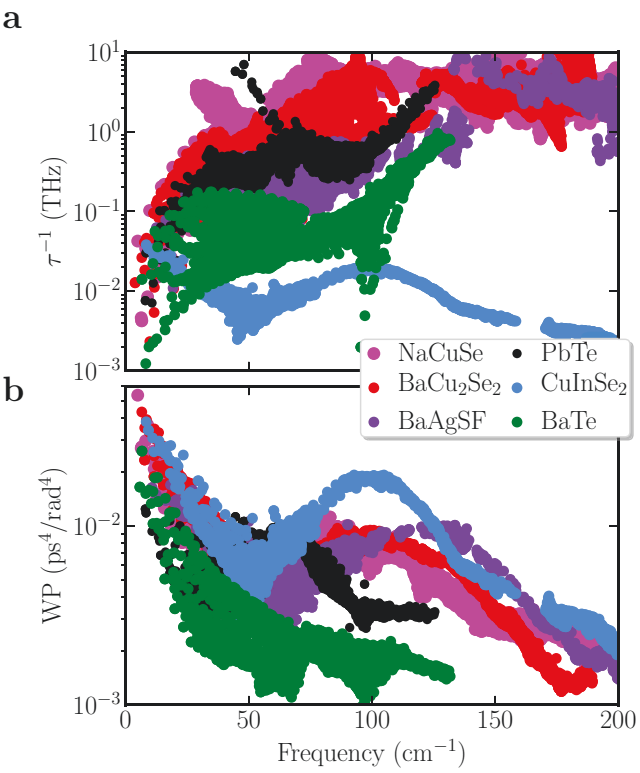

Figure 6. Anharmonic three-phonon interactions of the selected compounds. a) Phonon–phonon scattering rate (τ^{-1}) as a function of phonon frequency at room temperature. b) Weighted phase space at room temperature.

rates τ^{-1} of six compounds with similar v_m but different κ_L: BaTe (v_m = 2206 m s^{-1}; κ_L = 12.6 Wm^{-1} K^{-1}), $CuInSe_2$ (v_m = 2318 m s^{-1}; κ_L = 6.2 Wm^{-1} K^{-1}), PbTe (v_m = 2206 m s^{-1}; κ_L = 2.3 Wm^{-1} K^{-1}), BaAgSF (v_m = 2374 m s^{-1}; κ_L = 1.6 Wm^{-1} K^{-1}), $BaCu_2Se_2$ (v_m = 2236 m s^{-1}; κ_L = 0.87 Wm^{-1} K^{-1}), and NaCuSe (v_m = 2374 m s^{-1}; κ_L = 0.6 Wm^{-1} K^{-1}). Noticeably, the Cu/Ag compounds with edge-sharing polyhedra (BaAgSF, $BaCu_2Se_2$, and NaCuSe) have higher τ^{-1} in the low-frequency region than the corner-sharing $CuInSe_2$, and even rock-salt PbTe, a well known thermoelectric material with strong phonon anharmonicity.[72,75] In Figure 6b, we show the WP of three-phonon scattering in these compounds and we can see all these compounds have rather large WP, indicating high three-phonon transition probability. To relate the strong scattering rates to anharmonicity, we show in **Figure 7** the Grüneisen parameters (γ) and the ratios of third to second-order onsite force constants (OFC^{3rd}/OFC^{2nd}) of a subset of compounds with chalcopyrite (AMX_2), ZrCuSiAs-type ($AMXY$), and PbClF-type (AMX) structures. The γ characterizes the overall anharmonicity of a compound and OFC^{3rd}/OFC^{2nd} indicates the bond anharmonicity associated with a given ion. We see that high γ values are observed in the Cu/Ag compounds with edge-sharing tetrahedra, in line with the large OFC^{3rd}/OFC^{2nd} associated with Cu/Ag. Therefore, both low v_m and high τ^{-1} in the low-frequency region, which contribute to low κ_L, are associated with the weak *M*-*X* bond. It is known that compounds with a high CN generally have high anharmonicity[76] because of the large bond length between cation and anion, which is different from our bond weakening strategy. The compounds that satisfy our design rule have small CN (4) but with comparable or even higher phonon-phonon scattering rates and lower κ_L than rock-salt (CN = 8) BaTe and PbTe. This observation highlights the important role played by the unusual *p*-*d* coupling and edge/face-sharing polyhedra in phonon-phonon scattering. Furthermore, we also can see a considerable difference between corner-sharing and edge/face-sharing polyhedra by only inspecting the Cu/Ag based compounds as tabulated in Table 1 and Table S1, Supporting Information. As shown in Figure S2, Supporting Information, the different dependence of κ_L on v_m and $\overline{M}$ for the corner-sharing chalcopyrite and the edge/face-sharing polyhedral compounds (the rest compounds in the figure) clearly indicates that the compounds with edge/face-sharing polyhedra generally have low κ_L.

In order to simplify anharmonic phonon calculations, we excluded the compounds containing the cations with partially filled *d* orbitals, for example, compounds with both Cu^+ and Cu^{2+}. These compounds can have weak bonds as well because Cu^+/Ag^+ satisfy our strategy and Cu^{2+} can provide strong Coulomb repulsion when it is in the center of the edge/face-sharing polyhedron. For example, the face-sharing between $AgSe_4$ tetrahedron and $CrSe_6$ octahedron in $AgCrSe_2$ makes the Ag-Se bond so weak that the acoustic phonon modes are even dispersion-less and Ag^+ cations show superionic behavior,[77,78] and therefore it has an ultralow κ_L.[79] Moreover, as we can see from Table 1, there are only a few compounds for many of these prototype structures. It is very likely that some of these compounds have been synthesized but not included in the ICSD, and therefore are not explored here. Meanwhile, it is still possible that some of these compounds have not been fully characterized or synthesized yet. Therefore, we expect that many low κ_L compounds could be discovered by decorating these structures with elements that are similar to the existing ones, which has been commonly used to predict new compounds.[80,81]

With our material design strategy of suppressing κ_L, we can also rationally design as-yet synthesized thermoelectric materials by combining it with the methods focused on improving power factor. It is known that the *s*-orbital of the cations with lone-pair electrons can dramatically increase the band degeneracy of a semiconductor,[25] which is desired for enhancing power factors of thermoelectric materials.[82,83] Therefore, it is straightforward to explore new compounds by combining these two factors: edge/face-sharing MX_n (M = Cu^+ and Ag^+; X = pnictogens, chalcogenides, and halogens) polyhedra; cations with lone-pair electrons such as Tl^+, Pb^{2+}, and Bi^{3+}. Here, we take the ZrCuSiAs-type structure as an example to illustrate such a strategy. Our DFT calculations with element-substitutions in the ZrCuSiAs-type structure and other prototype structures of the $ABXY$ composition show that the lowest energy structure of PbCuSeF, PbAgSeF, and PbAgTeF has the ZrCuSiAs-type structure; they are dynamically stable, and their formation energies are close (<25 meV atom^{-1}) to the convex hull formed by the competing phases (see **Figure 8**), implying these compounds are likely synthesizable under the appropriate conditions. Further calculations reveal these compounds have relatively low κ_L (<1 Wm^{-1} K^{-1}). The band structures of these compounds are very similar to each other (see **Figure 9**). Both the valence band maximum (VBM) and conduction band

© 2021 Wiley-VCH GmbH

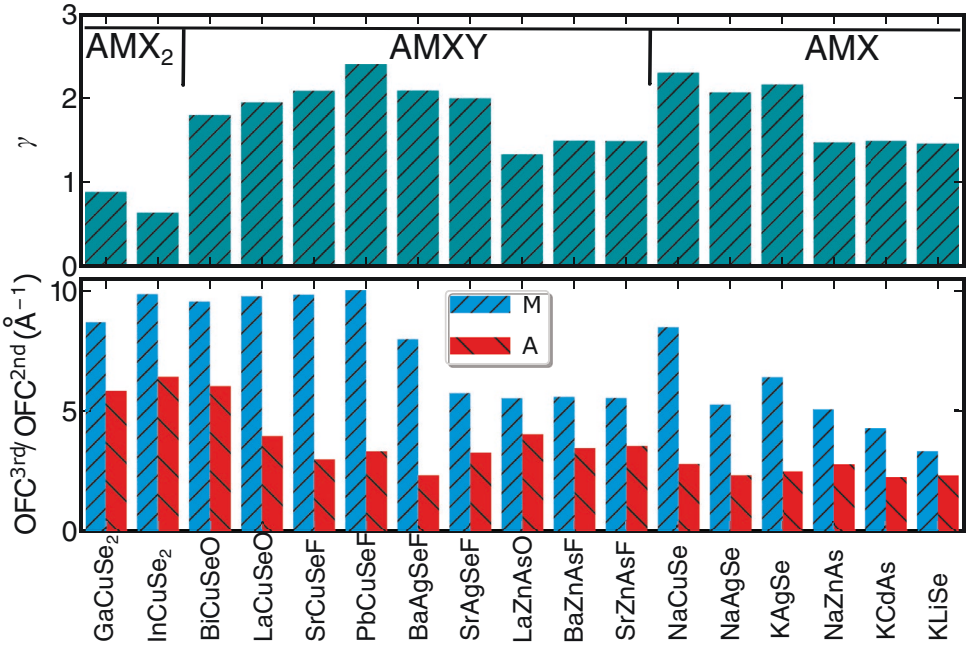

Figure 7. Grüneisen parameter γ and the ratio of third and second-order onsite force constants OFC^{3rd}/OFC^{2nd}. For simplicity, only the *A* and *M* cation sites OFC^{3rd}/OFC^{2nd} of chalcopyrite (AMX_2), ZrCuSiAs (*AMXY*), and PbClF-type (*AMX*) structures are plotted, where *X* and *Y* are anions.

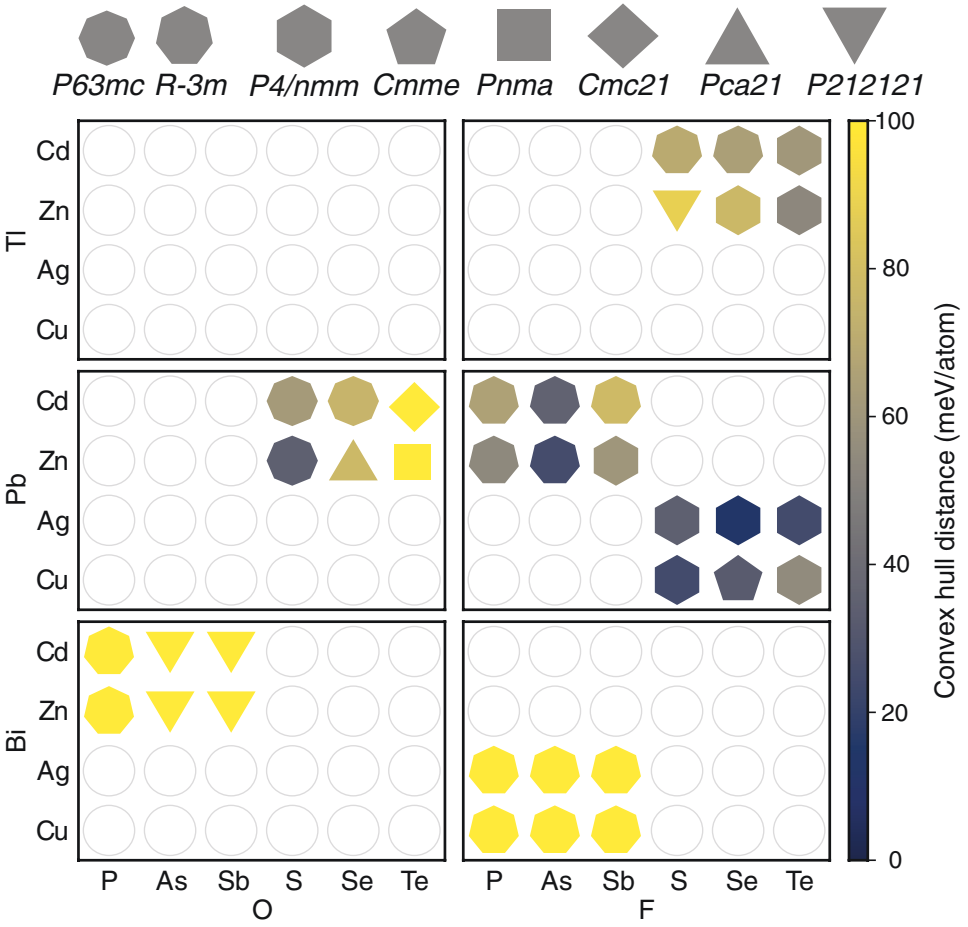

Figure 8. The heat map of the convex hull distance of *ABXY* compounds. White unfilled circles indicate that the corresponding compound is not charge balanced, and therefor is not studied. Other shapes (e.g., diamond, square, triangle, ...) represent the different symmetries of the respective ground state structure (see the legend at the top of the figure).

© 2021 Wiley-VCH GmbH

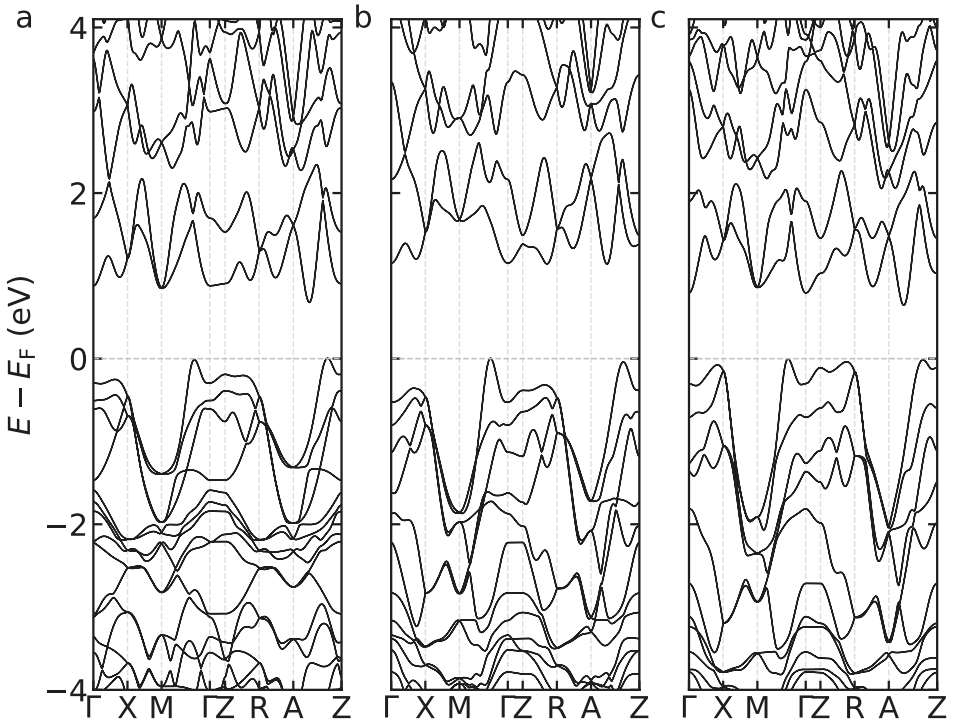

Figure 9. Electronic structures of Pb*MX*F (*M* =Cu and Ag; *X* = S, Se, and Te). a–c) Band structures of PbCuSeF, PbAgSeF, and PbAgTeF, respectively. The spin-orbital coupling is included.

minimum (CBM) are located in the middle of the lines between two high symmetry points (VBM: Σ line between Γ and M; CBM: *S* line between A and Z), where the valley degeneracy is 4, whereas the Ba analogs such as BaCuSeF and BaAgSeF have CBM and VBM at the Γ point with valley degeneracy of 1. Also, there are other valleys with energies close to VBM or CBM, which could further increase band degeneracy if the compounds can be properly doped. These characteristics resemble what has been observed in the excellent thermoelectric material BiCuSeO and other Bi-based compounds with the ZrCuSiAs-type structure, where the VBM and CBM are mainly from Bi 6*s* and 6*p* orbitals, respectively.[38,80] Our calculated power factors based on a simplified approach of computing electron-phonon coupling as implemented in the AMSET code[84] are shown in Figure S3, Supporting Information. The Pb-based compounds indeed have much higher power factors than the Ba-based ones at the same hole concentration. Similar exploration can be performed for the other structure types discovered in this work, and more promising thermoelectric materials could be potentially discovered.

4. Conclusion

In summary, we provide a feasible strategy of designing and discovering materials with low lattice thermal conductivities based on chemical bonding principles. The bond strength between Cu^+/Ag^+ and anions can be significantly weakened by filling the antibonding states originated from Cu/Ag-*d* and anion-*p* hybridization and enhancing Coulomb repulsion among cations in edge/face-sharing polyhedra. The consequence of the weak bond is the low speed of sound and high phonon-phonon scattering rates, which contribute to low lattice thermal conductivity ultimately. This approach is then used to screen the compounds collected in the ICSD, and 30 compounds with ultralow lattice thermal conductivities are discovered from thirteen prototype structures. We further introduce an approach to design thermoelectric materials by combining our thermal conductivity strategy with a known method of enhancing power factor. Three as-yet synthesized thermoelectric materials with low κ_L and high band degeneracy are discovered by combining a structure with low lattice thermal conductivity and cations with lone-pair electrons, Pb^{2+}. Our material design strategy of suppressing lattice thermal conductivity is straightforward to be extended to other materials as well.

5. Experimental Section

In this study, all DFT calculations are performed using the Vienna ab initio Simulation Package (VASP).[85,86] The projector augmented wave (PAW[87,88]) pseudo potential, plane wave basis set with 520 eV cutoff energy, and PBEsol[89] exchange-correlation functional were used. The qmpy[90,91] framework and the open quantum material database (OQMD)[90] was used for convex hull construction. Second-order force constants were computed by using the finite displacement method as implemented in the phonopy package.[92] Lattice thermal conductivities were calculated by solving the Boltzmann transport equation for phonons, as implemented in the ShengBTE code,[93] based on the second-order force constants calculated using phonopy and third-order

© 2021 Wiley-VCH GmbH

force constants calculated using thirdorder.py[94] and compressive sensing lattice dynamics.[95,96] For those materials exhibiting very low lattice thermal conductivities (<0.1 Wm^{-1} K^{-1}) from the phonon gas model, off-diagonal contributions to heat transfer were further accounted for using the recently developed unified theory of thermal transport following ref. [65]. Power factors of the selected materials are calculated by using the AMSET code,[84] and the acoustic deformation potential, ionized impurity, and polar optical phonon scattering to electrons are included.

The average sound velocity ν_m is calculated from bulk (B) and shear (G) moduli.[97]

$$\nu_m = \left[\frac{1}{3}\left(\frac{1}{\nu_L^3} + \frac{2}{\nu_T^3}\right)\right]^{-1/3} \quad (1)$$

$$\nu_T = \sqrt{\frac{G}{\rho}} \quad (2)$$

$$\nu_L = \sqrt{\frac{B + \frac{4}{3}G}{\rho}} \quad (3)$$

where ν_L and ν_T are longitudinal and transversal sound velocities, respectively, and ρ is mass density. The B and G are calculated from elastic constants. The mean values of Voigt and Reuss definition are adopted in this paper.

Supporting Information

Supporting Information is available from the Wiley Online Library or from the author.

Acknowledgements

J.H. and Y.X. contributed equally to this work. The authors acknowledge support by the U.S. Department of Energy, Office of Science and Office of Basic Energy Sciences, under Award No. DE-SC0014520 for lattice thermal conductivity calculations and the Center for Hierarchical Materials Design (CHiMaD) and from the U.S. Department of Commerce, National Institute of Standards and Technology, under Award No. 70NANB14H012 for materials screening. M.G.K. acknowledges support from the National Science Foundation through Grant DMR-2003476 for materials exploration work. This research used computer resources from the National Energy Research Scientific Computing Center, a DOE Office of Science User Facility supported by the Office of Science of the U.S. Department of Energy under Contract No. DE-AC02-05CH11231, the Extreme Science and Engineering Discovery Environment, which is supported by National Science Foundation grant number ACI-1548562, and the Quest high performance computing facility at Northwestern University.

Conflict of Interest

The authors declare no conflict of interest.

Data Availability Statement

The data that support the findings of this study are available from the corresponding author upon reasonable request.

Keywords

thermoelectric materials, lattice thermal conductivity, material design

Received: August 25, 2021
Revised: November 18, 2021
Published online: December 17, 2021

[1] G. A. Slack, *CRC Handbook of Thermoelectrics*, CRC Press, Boca Raton, FL **1995**, pp. 407–440.
[2] R. Darolia, *Int. Mater. Rev.* **2013**, *58*, 315.
[3] G. Wehmeyer, T. Yabuki, C. Monachon, J. Wu, C. Dames, *Appl. Phys. Rev.* **2017**, *4*, 041304.
[4] T. M. Tritt, *Thermal Conductivity: Theory, Properties, and Applications*, Springer Science & Business Media, Berlin **2005**.
[5] E. S. Toberer, A. Zevalkink, G. J. Snyder, *J. Mater. Chem.* **2011**, *21*, 15843.
[6] J. Mao, Z. Liu, J. Zhou, H. Zhu, Q. Zhang, G. Chen, Z. Ren, *Adv. Phys.* **2018**, *67*, 69.
[7] Z. Chen, X. Zhang, Y. Pei, *Adv. Mater.* **2018**, *30*, 1705617.
[8] K. F. Hsu, S. Loo, F. Guo, W. Chen, J. S. Dyck, C. Uher, T. Hogan, E. K. Polychroniadis, M. G. Kanatzidis, *Science* **2004**, *303*, 818.
[9] K. Biswas, J. He, I. D. Blum, C.-I. Wu, T. P. Hogan, D. N. Seidman, V. P. Dravid, M. G. Kanatzidis, *Nature* **2012**, *489*, 414.
[10] B. Poudel, Q. Hao, Y. Ma, Y. Lan, A. Minnich, B. Yu, X. Yan, D. Wang, A. Muto, D. Vashaee, X. Chen, J. Liu, M. S. Dresselhaus, G. Chen, Z. Ren, *Science* **2008**, *320*, 634.
[11] Y. Pei, J. Lensch-Falk, E. S. Toberer, D. L. Medlin, G. J. Snyder, *Adv. Funct. Mater.* **2011**, *21*, 241.
[12] E. J. Skoug, D. T. Morelli, *Phys. Rev. Lett.* **2011**, *107*, 235901.
[13] M. D. Nielsen, V. Ozoliņš, J. P. Heremans, *Energy Environ. Sci.* **2013**, *6*, 570.
[14] T. Tadano, Y. Gohda, S. Tsuneyuki, *Phys. Rev. Lett.* **2015**, *114*, 095501.
[15] T. Tritt, *Recent Trends in Thermoelectric Materials Research: Part Three*, Vol. 71, Elsevier, Amsterdam **2001**.
[16] G. S. Nolas, G. A. Slack, S. B. Schujman, in *Semiconductors and Semimetals*, Vol. *69*, Elsevier, Amsterdam **2001**, pp. 255–300.
[17] H. Lin, G. Tan, J.-N. Shen, S. Hao, L.-M. Wu, N. Calta, C. Malliakas, S. Wang, C. Uher, C. Wolverton, M. G. Kanatzidis, *Angew. Chem. Int. Ed.* **2016**, *55*, 11431.
[18] J. He, M. Amsler, Y. Xia, S. S. Naghavi, V. I. Hegde, S. Hao, S. Goedecker, V. Ozoliņš, C. Wolverton, *Phys. Rev. Lett.* **2016**, *117*, 046602.
[19] O. Delaire, J. Ma, K. Marty, A. F. May, M. A. McGuire, M.-H. Du, D. J. Singh, A. Podlesnyak, G. Ehlers, M. D. Lumsden, B. C. Sales, *Nat. Mater.* **2011**, *10*, 614.
[20] D. Sarkar, T. Ghosh, S. Roychowdhury, R. Arora, S. Sajan, G. Sheet, U. V. Waghmare, K. Biswas, *J. Am. Chem. Soc.* **2020**, *142*, 12237.
[21] T. Wang, Y. Xiong, Y. Wang, P. Qiu, Q. Song, K. Zhao, J. Yang, J. Xiao, X. Shi, L. Chen, *Mater. Today Phys.* **2020**, 100180.
[22] L. Pauling, *J. Am. Chem. Soc.* **1929**, *51*, 1010.
[23] S. L. Shindé, J. Goela, *High Thermal Conductivity Materials*, Vol. *91*, Springer, New York **2006**.
[24] D. Spitzer, *J. Phys. Chem. Solids* **1970**, *31*, 19.
[25] W. G. Zeier, A. Zevalkink, Z. M. Gibbs, G. Hautier, M. G. Kanatzidis, G. J. Snyder, *Angew. Chem., Int. Ed.* **2016**, *55*, 6826.
[26] D. T. Morelli, G. A. Slack, in *High Thermal Conductivity Materials*, Springer, New York **2006**, pp. 37–68.
[27] A. Togo, L. Chaput, I. Tanaka, *Phys. Rev. B* **2015**, *91*, 094306.
[28] D. L. Perry, *Handbook of Inorganic Compounds*, 2nd ed., CRC, Boca Raton, FL **2011**.
[29] G. A. Slack, P. Andersson, *Phys. Rev. B* **1982**, *26*, 1873.

© 2021 Wiley-VCH GmbH

[30] D. Morelli, V. Jovovic, J. Heremans, *Phys. Rev. Lett.* **2008**, *101*, 035901.
[31] S. Mukhopadhyay, D. Bansal, O. Delaire, D. Perrodin, E. Bourret-Courchesne, D. J. Singh, L. Lindsay, *Phys. Rev. B* **2017**, *96*, 100301.
[32] S. Hull, D. Keen, *J. Phys.: Condens. Matter* **1996**, *8*, 6191.
[33] K. Kurosaki, H. Uneda, H. Muta, S. Yamanaka, *J. Appl. Phys.* **2005**, *97*, 053705.
[34] L. Zhao, D. Berardan, Y. Pei, C. Byl, L. Pinsard-Gaudart, N. Dragoe, *Appl. Phys. Lett.* **2010**, *97*, 092118.
[35] T. Miller, J. Wittenberg, H. Wen, S. Connor, Y. Cui, A. Lindenberg, *Nat. Commun.* **2013**, *4*, 1369.
[36] A. C. Becauerel, *Ann. Chim. Phys.* **1827**, *35*, 328.
[37] P. Qiu, X. Shi, L. Chen, *Energy Storage Mater.* **2016**, *3*, 85.
[38] L.-D. Zhao, J. He, D. Berardan, Y. Lin, J.-F. Li, C.-W. Nan, N. Dragoe, *Energy Environ. Sci.* **2014**, *7*, 2900.
[39] H. Liu, X. Shi, F. Xu, L. Zhang, W. Zhang, L. Chen, Q. Li, C. Uher, T. Day, G. J. Snyder, *Nat. Mater.* **2012**, *11*, 422.
[40] X. Shi, F. Huang, M. Liu, L. Chen, *Appl. Phys. Lett.* **2009**, *94*, 122103.
[41] R. Nunna, P. Qiu, M. Yin, H. Chen, R. Hanus, Q. Song, T. Zhang, M.-Y. Chou, M. T. Agne, J. He, G. J. Snyder, X. Shi, L. Chen, *Energy Environ. Sci.* **2017**, *10*, 1928.
[42] P. Qiu, M. T. Agne, Y. Liu, Y. Zhu, H. Chen, T. Mao, J. Yang, W. Zhang, S. M. Haile, W. G. Zeier, J. Janek, C. Uher, X. Shi, L. Chen, G. J. Snyder, *Nat. Commun.* **2018**, *9*, 2910.
[43] T.-R. Wei, Y. Qin, T. Deng, Q. Song, B. Jiang, R. Liu, P. Qiu, X. Shi, L. Chen, *Sci. China Mater.* **2019**, *62*, 8.
[44] J. E. Jaffe, A. Zunger, *Phys. Rev. B* **1984**, *29*, 1882.
[45] S.-H. Wei, A. Zunger, *Phys. Rev. B* **1988**, *37*, 8958.
[46] Y. Zhang, Y. Wang, L. Xi, R. Qiu, X. Shi, P. Zhang, W. Zhang, *J. Chem. Phys.* **2014**, *140*, 074702.
[47] R. Woods-Robinson, Y. Han, H. Zhang, T. Ablekim, I. Khan, K. A. Persson, A. Zakutayev, *Chem. Rev.* **2020**, *120*, 4007.
[48] W. Li, N. Mingo, *Phys. Rev. B* **2015**, *91*, 144304.
[49] J. R. Sootsman, D. Y. Chung, M. G. Kanatzidis, *Angew. Chem., Int. Ed.* **2009**, *48*, 8616.
[50] K. Kamran, M. Anis-ur Rehman, A. Maqsood, *J. Phys. D: Appl. Phys.* **2007**, *40*, 869.
[51] W. Chen, J.-H. Pöhls, G. Hautier, D. Broberg, S. Bajaj, U. Aydemir, Z. M. Gibbs, H. Zhu, M. Asta, G. J. Snyder, B. Meredig, M. A. White, K. Persson, A. Jain, *J. Mater. Chem. C* **2016**, *4*, 4414.
[52] T. Tanishita, K. Suekuni, H. Nishiate, C.-H. Lee, M. Ohtaki, *Phys. Chem. Chem. Phys.* **2020**, *22*, 2081.
[53] X. Y. Shi, F. Q. Huang, M. L. Liu, , L. D. Chen, *Appl. Phys. Lett.* **2009**, *94*, 122103.
[54] T. Barth, *Zentralbl. Mineralogie, Geologie, Paläontologie, A* **1926**, *284*, 286.
[55] R. Heyding, *Can. J. Chem.* **1966**, *44*, 1233.
[56] R. D. Heyding, R. M. Murray, *Can. J. Chem.* **1976**, *54*, 841.
[57] M. Oliveria, R. McMullan, B. Wuensch, *Solid State Ionics* **1988**, *28*, 1332.
[58] G. Bergerhoff, R. Hundt, R. Sievers, I. D. Brown, *J. Chem. Inf. Comput. Sci.* **1983**, *23*, 66.
[59] A. Jain, S. P. Ong, G. Hautier, W. Chen, W. D. Richards, S. Dacek, S. Cholia, D. Gunter, D. Skinner, G. Ceder, K. A. Persson, *APL Mater.* **2013**, *1*, 011002.
[60] D. Waroquiers, X. Gonze, G.-M. Rignanese, C. Welker-Nieuwoudt, F. Rosowski, M. Göbel, S. Schenk, P. Degelmann, R. André, R. Glaum, G. Hautier, *Chem. Mater.* **2017**, *29*, 8346.
[61] Y. Xia, K. Pal, J. He, V. Ozoliņš, C. Wolverton, *Phys. Rev. Lett.* **2020**, *124*, 065901.
[62] Y.-L. Pei, J. He, J.-F. Li, F. Li, Q. Liu, W. Pan, C. Barreteau, D. Berardan, N. Dragoe, L.-D. Zhao, *NPG Asia Mater.* **2013**, *5*, 5e47.
[63] P. Vaqueiro, R. A. R. Al Orabi, S. D. Luu, G. Guelou, A. V. Powell, R. Smith, J.-P. Song, D. Wee, M. Fornari, *Phys. Chem. Chem. Phys.* **2015**, *17*, 31735.
[64] D. Fan, H. Liu, L. Cheng, J. Zhang, P. Jiang, J. Wei, J. Liang, J. Shi, *Phys. Chem. Chem. Phys.* **2017**, *19*, 12913.
[65] M. Simoncelli, N. Marzari, F. Mauri, *Nat. Phys.* **2019**, *15*, 809.
[66] J. Li, L.-D. Zhao, J. Sui, D. Berardan, W. Cai, N. Dragoe, *Dalton Trans.* **2015**, *44*, 2285.
[67] M. Luo, K. Bu, X. Zhang, J. Huang, R. Wang, F. Q. Huang, *Chem. Commun.* **2020**.
[68] Y. Xia, V. Ozoliņš, C. Wolverton, *Phys. Rev. Lett.* **2020**, *125*, 085901.
[69] S. Mukhopadhyay, D. S. Parker, B. C. Sales, A. A. Puretzky, M. A. McGuire, L. Lindsay, *Science* **2018**, *360*, 1455.
[70] M. A. McGuire, A. F. May, D. J. Singh, M.-H. Du, G. E. Jellison, *J. Solid State Chem.* **2011**, *184*, 2744.
[71] K. Kurosaki, K. Goto, H. Muta, S. Yamanaka, *J. Appl. Phys.* **2007**, *102*, 023707.
[72] Y. Xia, *Appl. Phys. Lett.* **2018**, *113*, 073901.
[73] W. Lee, H. Li, A. B. Wong, D. Zhang, M. Lai, Y. Yu, Q. Kong, E. Lin, J. J. Urban, J. C. Grossman, P. Yang, *Proc. Natl. Acad. Sci. U. S. A.* **2017**, *114*, 8693.
[74] H. Xie, S. Hao, J. Bao, T. J. Slade, G. J. Snyder, C. Wolverton, M. G. Kanatzidis, *J. Am. Chem. Soc.* **2020**, *142*, 9553.
[75] S. Lee, K. Esfarjani, T. Luo, J. Zhou, Z. Tian, G. Chen, *Nat. Commun.* **2014**, *5*, 1.
[76] S. A. Miller, P. Gorai, B. R. Ortiz, A. Goyal, D. Gao, S. A. Barnett, T. O. Mason, G. J. Snyder, Q. Lv, V. Stevanović, E. S. Toberer, *Chem. Mater.* **2017**, *29*, 2494.
[77] C. Wang, Y. Chen, *npj Comput. Mater.* **2020**, *6*, 26.
[78] L. Xie, J. Feng, R. Li, J. He, *Phys. Rev. Lett.* **2020**, *125*, 245901.
[79] D. Wu, S. Huang, D. Feng, B. Li, Y. Chen, J. Zhang, J. He, *Phys. Chem. Chem. Phys.* **2016**, *18*, 23872.
[80] J. He, Z. Yao, V. I. Hegde, S. S. Naghavi, J. Shen, K. M. Bushick, C. Wolverton, *Chem. Mater.* **2020**, *32*, 8229.
[81] K. Pal, Y. Xia, J. Shen, J. He, Y. Luo, M. G. Kanatzidis, C. Wolverton, *npj Comput. Mater.* **2021**, *7*, 82.
[82] Y. Pei, X. Shi, A. LaLonde, H. Wang, L. Chen, G. J. Snyder, *Nature* **2011**, *473*, 66.
[83] J. He, Y. Xia, S. S. Naghavi, V. Ozoliņš, C. Wolverton, *Nat. Commun.* **2019**, *10*, 719.
[84] A. M. Ganose, J. Park, A. Faghaninia, R. Woods-Robinson, K. A. Persson, A. Jain, *Nat. Commun.* **2021**, *12*, 2222.
[85] G. Kresse, J. Hafner, *Phys. Rev. B* **1993**, *48*, 13115.
[86] G. Kresse, J. Furthmülerb, *Comp. Mater. Sci.* **1996**, *6*, 15.
[87] P. E. Blöchl, *Phys. Rev. B* **1994**, *50*, 17953.
[88] G. Kresse, D. Joubert, *Phys. Rev. B* **1999**, *59*, 1758.
[89] J. P. Perdew, A. Ruzsinszky, G. I. Csonka, O. A. Vydrov, G. E. Scuseria, L. A. Constantin, X. Zhou, K. Burke, *Phys. Rev. Lett.* **2008**, *100*, 136406.
[90] J. Saal, S. Kirklin, M. Aykol, B. Meredig, C. Wolverton, *JOM* **2013**, *65*, 1501.
[91] S. Kirklin, J. E. Saal, B. Meredig, A. Thompson, J. W. Doak, M. Aykol, S. Rühl, C. Wolverton, *npj. Comput. Mater.* **2015**, *1*, 15010.
[92] A. Togo, F. Oba, I. Tanaka, *Phys. Rev. B* **2008**, *78*, 134106.
[93] W. Li, J. Carrete, N. A. Katcho, N. Mingo, *Comp. Phys. Commun.* **2014**, *185*, 1747.
[94] W. Li, L. Lindsay, D. A. Broido, D. A. Stewart, N. Mingo, *Phys. Rev. B* **2012**, *86*, 174307.
[95] F. Zhou, W. Nielson, Y. Xia, V. Ozoliņš, *Phys. Rev. Lett.* **2014**, *113*, 185501.
[96] F. Zhou, W. Nielson, Y. Xia, V. Ozoliņš, *Phys. Rev. B* **2019**, *100*, 184308.
[97] R. Hill, *Proc. Phys. Soc. Sect. A* **1952**, *65*, 349.

© 2021 Wiley-VCH GmbH